Acta Crystallographica Section B
Structural Science
ISSN 0108-7681

Structures of Fe^{II} spin-crossover complexes from synchrotron powder-diffraction data

Eva Dova,[a]* René Peschar,[a] Makoto Sakata,[b] Kenichi Kato,[c] Arno F. Stassen,[d]‡ Henk Schenk[a] and Jaap G. Haasnoot[d,e]

[a]University of Amsterdam, Faculty of Science, van 't Hoff Institute for Molecular Sciences, Laboratory for Crystallography, Nieuwe Achtergracht 166, NL-1018 WV Amsterdam, The Netherlands, [b]Department of Applied Physics, Nagoya University, Nagoya 464-8603, Japan, [c]Japan Synchrotron Radiation Research Institute, Hyogo 679-5198, Japan, [d]Leiden Institute of Chemistry, Leiden University, PO Box 9502, 2300 RA Leiden, The Netherlands, and [e]Technical University of Delft, Lorentzweg 1, 2628 CJ Delft, The Netherlands

‡ Current address: Kavli Institute of Nanoscience, Delft University of Technology, Lorentzweg 1, 2628 CJ Delft, The Netherlands.

Correspondence e-mail: eva@science.uva.nl

Received 5 June 2004
Accepted 23 June 2004

Crystal structure determination and analysis have been carried out for the two spin-crossover compounds $[Fe(teeX)_6](BF_4)_2$ (tee*X* is haloethyltetrazole; *X* = I: *teei*; *X* = Br: *teeb*), in both their high-spin (near 300 K) and their low-spin states (T = 90 K), using high-resolution powder-diffraction data collected at the ESRF (Grenoble, France) and SPring8 (Japan) synchrotron radiation facilities. The structures of *teei* have been solved using various direct-space structure determination techniques (grid search, genetic algorithm and parallel tempering) and refined with the Rietveld method using geometrical restraints. In the case of *teeb*, a structural model was found but a full refinement was not successful because of the presence of a significant amount of an amorphous component. Analysis of the structures (space group $P2_1/c$, Z = 2) and diffraction data, and the absence of phase transitions, show the overall structural similarity of these compounds and lead to the conclusion that the gradual spin-crossovers are likely to be accompanied by small structural changes only.

1. Introduction

At the molecular level, transition-metal complexes containing, for example, Fe^{II} can exist in a high-spin (HS, S = 2) or a low-spin (LS, S = 0) state. In some of these compounds, the spin state can be changed by external perturbation, such as a change of temperature or pressure or exposure to electromagnetic radiation (Gütlich *et al.*, 1994; Gütlich & Hauser, 1990; Decurtins *et al.*, 1984, 1985; Meissner *et al.*, 1983), and this property may find future applications in data storage or display devices (Gütlich *et al.*, 2000; Kahn & Jay Martinez, 1998; Kröber *et al.*, 1993). In the solid state, the magnetic spin-crossover (SCO) behaviour is in general monitored by ^{57}Fe Mössbauer spectroscopy and magnetic susceptibility measurements. A wide range of SCO behaviour has been encountered: for example, gradual, complete, two-step transitions, transitions with a residual HS species at low temperature and hysteresis loops (Stassen *et al.*, 2003; Guionneau *et al.*, 1999; Real *et al.*, 1997).

Several theoretical models have been developed that explain the observed variation of the SCO transition curves. The regular solution model was proposed by Slichter & Drickamer (1972) and developed further by, among others, Onishi & Sugano (1981) and Spiering *et al.* (1982). In this model and these papers it is claimed that the origin of the intermolecular interactions lies in the elasticity of the medium. A volume change of a few molecules uniformly distributed over the crystal, by replacing atoms of different size or by the spin-state change of spin-crossover molecules, may give rise to lattice strain and this, in turn, to long-range interactions. This

effect may be interpreted as an internal pressure that increases linearly with the concentration of the LS species and affects all molecules in the crystal in the same way (independent of distances). Assuming elastic interactions in the solid state, a continuum model was proposed in order to model the non-ideality of the transition curves (Gütlich *et al.*, 1994).

In another theoretical model, proposed by Sorai & Seki (1974), the LS and HS molecules are assumed not to be distributed randomly but to form domains with the same spin. These authors suggested that the SCO occurs simultaneously in a group of molecules that form a 'cooperative' region. Bolvin & Kahn (1995) explored this possibility with Monte Carlo simulations in the above case. These authors concluded that molecules with the same spin tend to assemble themselves in clusters, a direct result of high cooperativity, and they stated that these clusters should be viewed in terms of a high probability and not of a static distribution.

Recently, SCO transitions have been described quantitatively taking into account nearest-neighbour interactions (specific and non-specific molecular interactions) and ordering, the latter being defined as the possibility of the formation of regular structures with alternating HS and LS structures (Koudriavtsev *et al.*, 2003*a*,*b*).

Recently, a novel class of SCO Fe^{II} complexes was introduced, with halogen-substituted ethyltetrazoles as ligands (Stassen *et al.*, 2002, 2003). Depending on the substituted halogen (F, Cl, Br or I), anion (BF_4^- and ClO_4^-) and preparation method, a wide variety of magnetic behaviour was observed. Since single crystals could be obtained for none of these compounds, a project was started to solve their structures from powder-diffraction data. For $[Fe(teec)_6](BF_4)_2$ [teec is 1-(2-chloroethyl)tetrazole; hereafter *teec*], which shows a two-step HS-to-LS transition, both room-temperature (HS; Dova *et al.*, 2001) and low-temperature (LS) crystal structure models have been obtained (Dova, 2003).

In this paper, we report the crystal structures of $[Fe(teei)_6](BF_4)_2$ (hereafter *teei*) in the HS state [at room temperature (RT)] and in the LS state (90 K). We also present the general structural features of $[Fe(teeb)_6](BF_4)_2$ (hereafter *teeb*) in the HS state (300 K) and in the LS state (90 K). According to magnetic susceptibility measurements and ^{57}Fe Mössbauer spectroscopy, both *teei* and *teeb* show a (almost) complete gradual SCO with transition temperatures of $T_{1/2}$ = 205 and 166 K, respectively (Fig. 1; Stassen *et al.*, 2003).

From an analysis of the structures in relation to their SCO behaviour it is concluded that in these compounds the SCO is accompanied by only small structural changes.

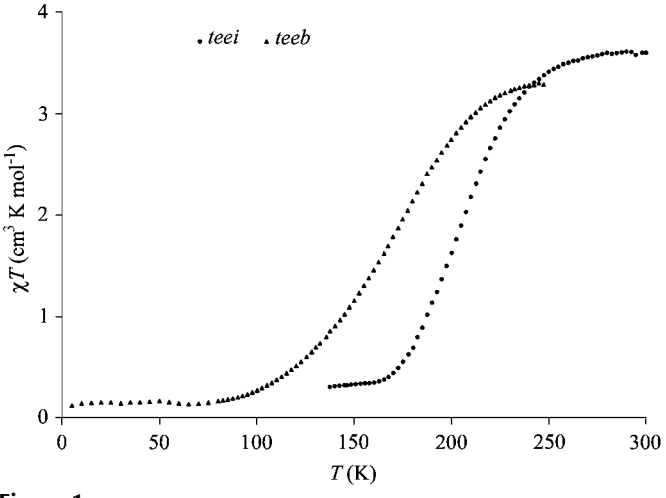

Figure 1
Molar magnetic susceptibility (χT) *versus* temperature (T) of $[Fe(teei)_6](BF_4)_2$ and $[Fe(teeb)_6](BF_4)_2$.

2. Experimental

Both *teei* and *teeb* are white crystallites, which were synthesized as described by Stassen (2002). Data sets at RT were collected at beamline BM01B at the European Synchrotron Radiation Facility (Grenoble, France), with λ = 0.75003 Å (hereafter ESRF data). Samples were measured in capilllaries (0.5 mm diameter) and rotated during the measurement. Data were taken by continuously scanning the interval $3.03 < 2\theta < 43.26°$ and were finally binned at 0.005° 2θ.

Temperature-dependent data-set series were collected at beamline BL02B2 of SPring8 at the Japan Synchrotron Radiation Research Institute (Nishi-Harama, Hyogo, Japan; called hereafter SPring8 data), using λ = 0.999995 Å. A large Debye–Scherrer camera (radius 286.5 mm) was available, together with an N_2 gas flow for low-temperature data collection (90–300 K; accuracy ±1–2 K; Nishibori *et al.*, 2001). An imaging-plate (IP) detector was mounted on the 2θ arm. Selecting an IP pixel size of 50 µm and using a long vertical slit in front of the IP, up to 18 different powder patterns could be collected on a single IP. A 0.4 mm capillary was mounted in the sample holder and rotated with a speed of 6° min^{-1}. After each experiment, the IP was read out by a BAS-2500 machine and a two-dimensional digital frame was created, from which the 2θ *versus* intensity powder-diffraction patterns ($0.01 < 2\theta < 76.61°$, step 0.01°) were obtained with the program *Ipv*32 (SPring8, local program) by integrating 51 pixels of the image, which correspond to 2.55 mm on the IP.

Short exposures (5 min) of several samples were used to examine the quality of the powder. Almost all samples were rather granular; this situation was difficult to avoid because the compounds were very hard and difficult to grind. Using the best samples, short-scan data (5 min) were taken at 300 K and from 250 to 90 K in steps of 10 K. To avoid temperature overshoot, a temperature-stabilization period of 5 min was applied before starting data collection. Long-term data collection (60 min) was carried out at selected temperatures, including 300 and 90 K, using the same temperature-stabilization period. After the long-term experiments, the colours of the samples had turned to brown (*teei*) and orange (*teeb*).

In the SPring8 diffraction patterns of *teei*, several broad intensity peaks can be observed that are not present in the ESRF data. These peaks are attributed to impurities present in the batch prepared for the experiments at SPring8 (the batch used for the experiments at the ESRF was no longer available), and 2θ ranges corresponding to these peaks have been

Table 1
Experimental details for $[Fe(teei)_6](BF_4)_2$.

$R_p = \sum|y_{obs} - y_{calc}|/\sum y_{obs}$; $r_{wp} = [\sum w(y_{obs} - y_{calc})^2/\sum wy_{obs}^2]^{1/2}$. $\chi^2 = [\sum w(y_{obs} - y_{calc})^2/(N - P)]^{1/2}$; N is the number of observations and P is the number of variables. The first line for the 2θ region, R_p and R_{wp} list the settings and results of the *GSAS* refinement. The second line for the 2θ region, R_p and R_{wp} list the settings and results of the FPD procedure.

	ESRF (RT)	SPring8 90 K
Crystal data		
Chemical formula	$[Fe^{2+}(C_3H_5N_4I)_6](BF_4)_2^-$	$[Fe^{2+}(C_3H_5N_4I)_6](BF_4)_2^-$
Chemical formula weight	1573.50	1573.50
Space group	$P2_1/c$	$P2_1/c$
a (Å)	12.64250 (19)	12.3177 (3)
b (Å)	18.0349 (3)	17.6766 (4)
c (Å)	10.64881 (16)	10.4685 (3)
β (°)	90.3080 (11)	90.5991 (17)
V (Å^3)	2427.95 (7)	2279.25 (12)
Z	2	2
Wavelength (Å)	0.75003	0.999995
D_x (Mg m^{-3})	2.154	2.293
Temperature (K)	293	90
Data collection		
Diffractometer	BM01B at ESRF	BL02B2 at SPring8
2θ region (°)	3.03–38.03	3.0–51.0
	3.03–25.03	3.0–30.0
Excluded regions (°)		12.85–12.95
		18.38–18.54
No. of variables	187	212
R_p	0.0522	0.0252
	0.0724	0.0197
R_{wp}	0.060	0.0367
	0.1120	0.0327
χ^2	3.96	10.34

excluded in order to improve the unit-cell refinement in the case of the 300 K data; in the case of the 90 K data, this exclusion was not considered to be necessary. Moreover, in the 90 K data set, 2θ regions corresponding to ice peaks were excluded, except for ice peaks very close to reflection peaks. Table 1 lists experimental data while Fig. 2 shows the RT and 90 K patterns of *teei*.

In the diffraction patterns of *teeb*, a significant amorphous component is present, resulting in a decrease of peak intensities and broadening of the peak profiles mainly in the range $12 < 2\theta < 18°$. Therefore, four regions (not including any reflection position) have been excluded in order to improve the refinement (Table 2 gives experimental data for *teeb*).[1]

3. Structure solution and refinement methods

3.1. Structure solution

All powder-diffraction patterns were indexed using the program *ITO* (Visser, 1969). The ESRF data were decomposed with the full-pattern decomposition (FPD) module of the program *MRIA* (Zlokazov & Chernyshev, 1992) using a split-type pseudo-Voigt profile function (Toraya, 1986) into X_{obs} values [X_{obs} is the intensity of a resolved reflection or the sum intensity of a cluster of reflections; see Chernyshev & Schenk (1998)]. The background was divided into three segments and each one was fitted with a Legendre polynomial (up to fifth order). The unit cells of the SPring8 patterns were refined with the Pawley refinement as incorporated into the *Materials Studio* package (*MS*; Accelrys, 2001). The background was fitted with the default settings (20th-order polynomial). At first, the Pearson-VII profile function was used to fit the patterns. These fitted patterns were used in all cases in the first run of the structure solution procedure. Later, the Tomandl pseudo-Voigt profile function was used, offering a more satisfactory fitting, and this profile function was used for additional structure solution runs (if any) and for all Rietveld refinement runs. In some cases, an asymmetry correction was applied according to the Bérar–Baldinozzi function (Bérar & Baldinozzi, 1993). All unit cells were established to be monoclinic and the space group assigned in all cases was $P2_1/c$.

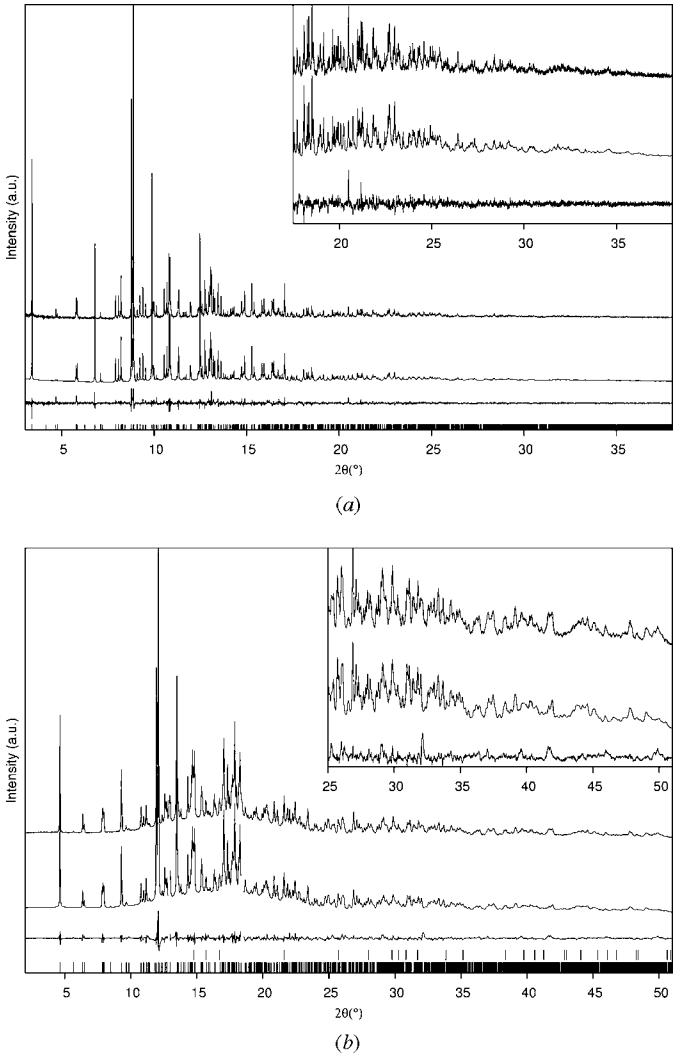

Figure 2
Rietveld refinement (*GSAS*) final plots of $[Fe(teei)_6](BF_4)_2$ (*a*) at RT and (*b*) at 90 K: experimental diffraction pattern (upper), the pattern as calculated from the refined crystal structure (middle), the difference between these patterns (lower), ice peaks (upper row of vertical lines) and reflection positions (lower row of vertical lines).

[1] Supplementary data for this paper are available from the IUCr electronic archives (Reference: NA5021). Services for accessing these data are described at the back of the journal.

Table 2
Experimental details for $[Fe(teeb)_6](BF_4)_2$.

$R_p = \sum|y_{obs} - y_{calc}|/\sum y_{obs}$; $r_{wp} = [\sum w(y_{obs} - y_{calc})^2/\sum wy_{obs}^2]^{1/2}$. $\chi^2 = [\sum w(y_{obs} - y_{calc})^2/(N - P)]^{1/2}$; N is the number of observations and P is the number of variables. The first line for the 2θ region, R_p and R_{wp} list the settings and results of the *GSAS* refinement. The second line for the 2θ region, GoF, R_p and R_{wp} list the settings and results of the FPD procedure.

	SPring8 300 K (M1)	SPring8 300 K (M2)	SPring8 90 K (M1)
Crystal data			
Chemical formula	$[Fe^{2+}(C_3H_5N_4Br)_6](BF_4)_2^-$	$[Fe^{2+}(C_3H_5N_4Br)_6](BF_4)_2^-$	$[Fe^{2+}(C_3H_5N_4Br)_6](BF_4)_2^-$
Chemical formula weight	1291.53	1291.53	1291.53
Space group	$P2_1/c$	$P2_1/c$	$P2_1/c$
a (Å)	12.2832 (6)	12.2595 (10)	11.9297 (7)
b (Å)	18.0705 (15)	18.1098 (13)	17.8169 (8)
c (Å)	10.4766 (3)	10.4607 (11)	10.2874 (3)
β (°)	90.106 (3)	90.013 (12)	89.992 (2)
V (Å^3)	2325.4 (2)	2322.5 (4)	2186.59 (17)
Z	2	2	2
Wavelength (Å)	0.999995	0.999995	0.999995
D_x (Mg m^{-3})	1.844	1.847	1.962
Temperature (K)	300	300	90
Data collection			
Diffractometer	BM01B at ESRF	BL02B2 at SPring8	BL02B2 at SPring8
2θ region (°)	3.03–38.03 3.03–25.03	3.0–50.0 3.0–30.0	3.0–51.0 3.0–30.0
Excluded regions (°)	13.15–13.25, 13.57–13.75, 16.83–16.93, 17.03–17.23	13.15–13.25, 13.57–13.75, 16.83–16.93, 17.03–17.23	13.10–13.45, 13.83–13.95, 17.16–17.32, 17.43–17.58
No. of variables	184	180	181
R_p	0.0456 0.0246	0.0638 0.0246	0.0505 0.0258
R_{wp}	0.0649 0.0407	0.0883 0.0407	0.0697 0.0398
χ^2	40.77	75.51	43.85

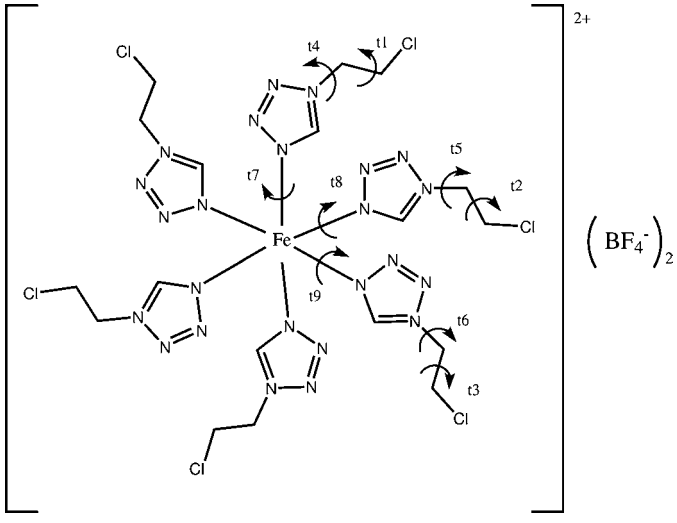

Figure 3
Definition of torsion angles ($t1$–$t9$) in $[Fe(teei)_6](BF_4)_2$ and $[Fe(teeb)_6](BF_4)_2$.

Table 3
Subsearches in the grid-search solution of $[Fe(teei)_6](BF_4)_2$.

Subsearch	No. of X_{obs}	Fragment	Parameters	Amount of DOF	Step sizes (initial, final)	Final $R(X)$
Rotation angle	90	$(teei)_3$	$\phi\psi\kappa$	3	10°, 1°	0.611
Torsion angle	90	$(teei)_3$	Sets $t1$–$t3$, $t4$–$t6$, $t7$–$t9$	3	10°	0.560
	120	$(teei)_3$	$t1, \ldots, t9$	9	10°, 1°	0.363
Rotation and translation	120	BF_4	x, y, z	6	0.4 Å, 0.05 Å	0.281
			φ, ψ, κ		10°, 1 Å	
Rotation	120	$(teei)_3$	φ, ψ, κ	3	10°, 1°	0.260

Taking into account the space group ($P2_1/c$) and volume requirements ($Z = 2$), the molecule was assumed to be centrosymmetric and, with the metal kept fixed in a special position [(0, 0, 0) was used], but only half of the molecule was required as a search model; the model thus comprises two fragments: the $(teeX)_3$ moiety and the BF_4^- ion. This structural model is characterized by 18 degrees of freedom (DOF): three rotational parameters and nine torsion angles for the $(teeX)_3$ moiety, and six parameters (three translational and three rotational) for the BF_4^- ion (Fig. 3). The initial search model for all the applied techniques was constructed from the structure of *teec* (Dova *et al.*, 2001), with Cl replaced by I and Br for the *teei* and *teeb* complexes, respectively.

The structure of *teei* at RT was solved from ESRF data by dividing the total grid-search problem into several smaller subsearches (Dova *et al.*, 2001; Dova, 2003): (*a*) a rotational search to position the $(teei)_3$ moiety (three DOF), (*b*) a torsion-angle search to establish the orientation of the tetrazole rings and the iodoethyl groups (Fig. 3; $t1$–$t9$; nine DOF), and (*c*) a translational and rotational search (six DOF) to locate the BF_4^- ion (see Table 3). The search order followed was (*a*), (*b*), (*c*), (*a*).

Torsion-angle searches exploiting 90 X_{obs} values were made in order to determine more accurately the position of the rings and the iodoethyl side chains. Initially, the torsion angles were arranged in three groups, $t1$–$t3$, $t4$–$t6$ and $t7$–$t9$, which were handled independently, and searches in steps of 10° in the whole torsion-angular range were applied. Two structural models were found, with almost the same $R(X)$. In order to distinguish between the two models, additional torsion-angle searches using 100, 120 and 160 X_{obs} values were applied. After inspection of the results, it was concluded that the above-mentioned structural models were better distinguished [in terms of $R(X)$ values] in the search with 120 X_{obs} values and therefore it was decided to continue the grid search using 120 X_{obs} values.

Structures of *teei* and *teeb* at 300 and 90 K (SPring8 data) have been solved with parallel tempering, as incorporated into *Powder Solve* (Engel *et al.*, 1999) of *MS*, using default settings unless stated otherwise. The $(teeX)_3$ moiety and the BF_4^- ion were searched for simultaneously in the first run. At 90 K, the Fe—N bonds of the initial model of *teei* were shortened to

2.2 Å before carrying out the parallel tempering runs. The search was performed using the interval 3–25° 2θ unless stated otherwise.

3.2. Structure refinement

Rietveld refinement (RR) of the ESRF data model of *teei* was carried out using the program *MRIA*. The background parameters were refined (fifth-order Legendre polynomial), a split-type pseudo-Voigt profile (Toraya, 1986) was assigned to the reflections and texture correction was applied using the symmetrized-harmonics expansion method (Ahtee *et al.*, 1989; Järvinen, 1993). Zero-point correction and cell-parameter refinement were also carried out. In order to avoid distortion of the fragments, a distance-restrained refinement was applied to intramolecular distances (< 6 Å) with σ = 1% of the ideal distance.

A limited RR of the SPring8 300 and 90 K models of *teei* and *teeb* was carried out with the *MS* package. The Tomandl pseudo-Voigt profile function was used and, in some cases, an asymmetry correction was applied according to the Bérar–Baldinozzi function. A texture correction was applied using the March–Dollase method. The initial values of the parameters *a**, *b**, *c** and *r* were found by simulated annealing (as incorporated into the *MS* package) and then refined with RR. The Fe(tee*X*)$_6^{2+}$ moiety and BF_4^- ion were refined initially as rigid bodies; the torsion angles (see Fig. 3) were also refined. Attempts to relax the rigid-body restraints and to refine individual atomic coordinates were not successful and resulted in a distortion of the model. In view of these results, it was decided to continue the RR with the program *GSAS* (Larson & Von Dreele, 1994) using the interface *EXPGUI* (Toby, 2001). A special type of pseudo-Voigt function (profile function type 3 in *GSAS*) was used to model reflection asymmetry. Texture was corrected for using a spherical harmonics function up to sixth order. Zero-point correction and cell-parameter refinement were also applied. Bond-distance, bond-angle and planar restraints were applied in order to avoid extreme distortion of the structural model.

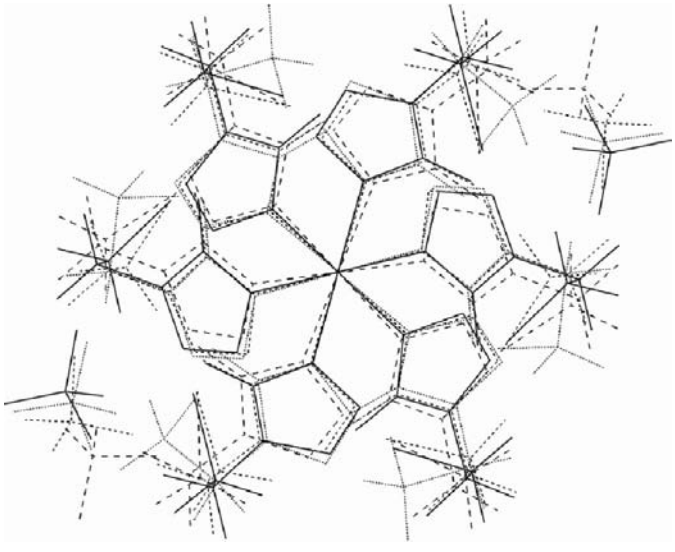

Figure 4
The structural models of $[Fe(teei)_6](BF_4)_2$ obtained after grid search (···), genetic algorithm (– –), parallel tempering techniques (- - -) and local grid search (—).

4. Results and discussion

4.1. Indexing and analysis of scan *versus* long-term data

The ESRF patterns and all the long-term SPring8 patterns of *teei* and *teeb* could be indexed as monoclinic, and on the basis of the expected similarity with the *teec* complexes, as suggested by the similarity of the diffraction patterns, $P2_1/c$ was assumed to be the most likely space group, with $Z = 2$ in view of the available cell volume (Tables 1 and 2). The diffraction patterns of the scan measurements of *teei* and *teeb* as a function of decreasing temperature (300 → 90 K) showed only slight and gradual changes of the intensities and peak positions, the latter indicating a gradual lattice contraction. Comparison of the scan and long-term measurements at the same temperature revealed hardly any difference, except for the somewhat broader peaks in the scan patterns of *teei*. This broadening has been attributed to the extensive grinding of the sample used for the scan measurements. Thus, it is concluded that no significant crystallographic phase transition has taken place and that, under the time scales used (scan 5 min, long-term 60 min), different types of unit cells do not occur, in contrast to the cases of *teec* and $[Fe(teec)_6](ClO_4)_2$ (Dova, 2003).

4.2. Structure solution and refinement of *teei*

The grid-search procedure for *teei* at RT, summarized in Table 3, finally led to a model [$R(X)$ = 0.26] that could subsequently be refined using RR in *MRIA* (see Table 1).

For the SPring8 data, after the first parallel tempering run (18 DOF), the structural model found was already well located, with R_{wp} values of 0.0758 and 0.0578 at 90 and 300 K, respectively.

A comparison of the structural models of *teei* resulting from the grid search, parallel tempering (at 300 K) and a genetic algorithm implementation in *MRIA* (data not shown) revealed them to be largely the same, except for the position of the C atom bonded to the I atom in all three ligands (Fig. 4). Therefore, a local grid search was performed (90 X_{obs} values) around the position of the structural model delivered by parallel tempering. This local grid search comprised a variation of all torsion angles within a range of ±20° in steps initially of 4° and finally of 1°, a search of the BF_4^- ion with final translation steps of 0.01, 0.02 and 0.01 Å within ranges of ±0.63, ±0.90 and ±0.53 Å along the *a*, *b* and *c* axes, respectively, and a rotation in steps of 1° within ±4° around φ, ψ and κ. The final model [$R(X)$ = 0.249] after this local grid search was processed with RR in *MRIA* and turned out to be very similar to the solution found by parallel tempering. It is judged, though, that the differences between all those models can become insignificant after RR.

The results of the RR of all models are summarized in Table 1. Results obtained with each of the programs will be discussed below.

MRIA ESRF data. In order to avoid distortion of the fragments, a distance-restrained refinement was carried out, using restraints for all intramolecular distances (< 6 Å) with $\sigma = 1\%$ of the ideal distance. The ideal C—I distance was set to 2.16 Å and all other distance restraints involving the I atom were removed. The weight c_w, which weighs the residual distance restraints function, S_R, *versus* the Rietveld residual function, S_Y, was gradually reduced from 317.4 to 2.96. Attempts to lower c_w any further resulted in a distortion of the model. The atomic displacements of the I, C and N atoms were refined isotropically and constrained to be equal within each of the following three groups: I atoms, C and N atoms of all three tetrazole rings, and C atoms of every ethyl group separately. Atomic displacement parameters of Fe, B and F were fixed to 0.025, 0.05 and 0.10 Å, respectively. The final plot of the observed, calculated and difference patterns is shown in Fig. 2(*a*).

GSAS 90 K (SPring8 data). As discussed, the final RR of the 90 K model was carried out with *GSAS*. The hexagonal ($P6_3/mmc$) phase of ice, with $a = b = 4.523$ Å and $c = 7.367$ Å (Megaw, 1934), was introduced as a second phase into the RR. After fitting the ice phase, using the same profile function as for the main phase, all of the parameters were kept constant and only the parameters of *teei* were refined. Two regions were excluded (12.85–12.95 and 18.38–18.54° 2θ) for reasons discussed in §2. Bond-distance, bond-angle and planar restraints were applied, and every group of restraints contributed to the final χ^2, as shown in Table 4. Atomic displacement parameters of the Fe and I atoms were refined isotropically, the atomic displacement parameters of the I atoms being constrained to be equal. Atomic displacement parameters of the other non-H atoms could not be refined and were kept constant at 0.025 Å^2. Spherical harmonics coefficients up to 12th order were refined, leading to a final texture index $J = 1.483$, implying a moderate preferred orientation. The final plot of the observed, calculated and difference patterns is shown in Fig. 2(*b*). The larger differences in the RR plot of the structure at 90 K are concentrated mainly at the ice peaks and at the peaks attributed to impurities (either excluded or not).

4.3. Structure solution and refinement of *teeb*

It was difficult to obtain convincing structural models of *teeb* suitable for refinement. A large amorphous contribution in all diffraction patterns of *teeb* is considered to be the main reason for this difficulty. In the case of the ESRF data all attempts to find suitable models failed, but for the 300 and 90 K SPring8 data some models were found with parallel tempering, although with difficulty. At 300 K, two parallel tempering runs were carried out because the solution of the first run gave interatomic contacts that were too short. The second run solution was processed in the RR of *MS*, in spite of the relatively high R_{wp} value (0.159). The structural model found at 90 K ($R_{wp} = 0.171$) was very similar to this second 300 K model. Attempts to obtain a model with a lower R_{wp} were not successful.

Table 4
Terms in the least-squares minimization of the Rietveld refinement (*GSAS*) and the final values of the global weighting factors (f_d, f_a, f_p) of $[Fe(teei)_6](BF_4)_2$ (90 K) and $[Fe(teeb)_6](BF_4)_2$ at 300 K (M1 and M2) and 90 K.

	$[Fe(teei)_6](BF_4)_2$	$[Fe(teeb)_6](BF_4)_2$		
T (K)	90	300 (M1)	300 (M2)	90 (M1)
Bond distances (46)	816.54	5355.6 (52 restr.)	7894.4	7366.4
f_d	2	25	25	20
Bond angles (78)	390.60	7627.7	13313	17039
f_a	16	15	15	70
Planar Group (15)	880.39	2136.6	6303.4	5855.1
f_p	2	25	35	35
Total data (powder + restraints)	49 609 (5010 obs.)	195 520 (4980 obs.)	362 240 (4980 obs.)	268 180 (6292 obs.)

As discussed above, eventually the models at 300 and 90 K were refined with *GSAS*. Because of the difficulties in obtaining convincing structural models and in view of the expected isomorphism of *teeb* to the structures of *teec* (Dova, 2003) and *teei*, as suggested by the similarity of the diffraction patterns, two structural models were processed with the RR in *GSAS*: the (300 K) M1 model, as obtained from the RR with *MS*, and model M2, taken from Dova *et al.* (2001) with the Cl atoms replaced by Br atoms In the refinements of M1 and M2 the same procedure was followed. The structural models before and after RR are plotted in Fig. 5. The results of RR with *GSAS* are listed in Table 2. The final values of the global weighting factors and every group of restraints contributed to the final χ^2, as shown in Table 4. The criteria-of-fit (Table 2) and the difference patterns (Figs. 6*a* and 6*b*) suggested M1 to be the best structural model. For this reason and because the structural model at 90 K found by parallel tempering was similar to M1 (Fig. 5), M1 was taken as the starting model for the refinement at 90 K, applying the same procedure as at 300 K (Tables 2 and 4).

The final plots of the observed, calculated and difference patterns (Fig. 6*c*) show a relatively poor agreement between the calculated and experimental patterns in the range $12 < 2\theta < 18°$, where the contribution of the amorphous component is significant and the intensities of the phase under investigation are low with broad profile shapes. This poor agreement is considered to be the main reason for the high values of the texture index, implying that not only the texture but also other effects are modelled. Although the refinements of *teeb* cannot be considered completely satisfactory, the general structural features are similar to those of *teei.* A more crystalline sample would be required for a more satisfactory structure refinement.

Table 5
Selected bond distances and angles of $[Fe(teei)_6](BF_4)_2$ at RT (ESRF data) and 90 K (SPring8 data) and of $[Fe(teeb)_6](BF_4)_2$ at 300 and 90 K (SPring8 data).

	$[Fe(teei)_6](BF_4)_2$		$[Fe(teeb)_6](BF_4)_2$	
T	RT	90 K	300 K	90 K
Fe—N4*a*	2.200 (15)	2.046 (18)	2.222 (6)	2.098 (4)
Fe—N4*b*	2.219 (15)	1.970 (18)	2.226 (5)	1.970 (9)
Fe—N4*c*	2.215 (16)	1.873 (17)	2.220 (7)	2.079 (9)
N4*a*—Fe—N4*b*	90.3 (6)	91.2 (7)	87.6 (3)	93.7 (4)
N4*a*—Fe—N4*c*	90.7 (6)	91.3 (8)	88.2 (2)	96.5 (3)
N4*b*—Fe—N4*c*	90.2 (6)	90.7 (7)	91.2 (3)	85.8 (3)

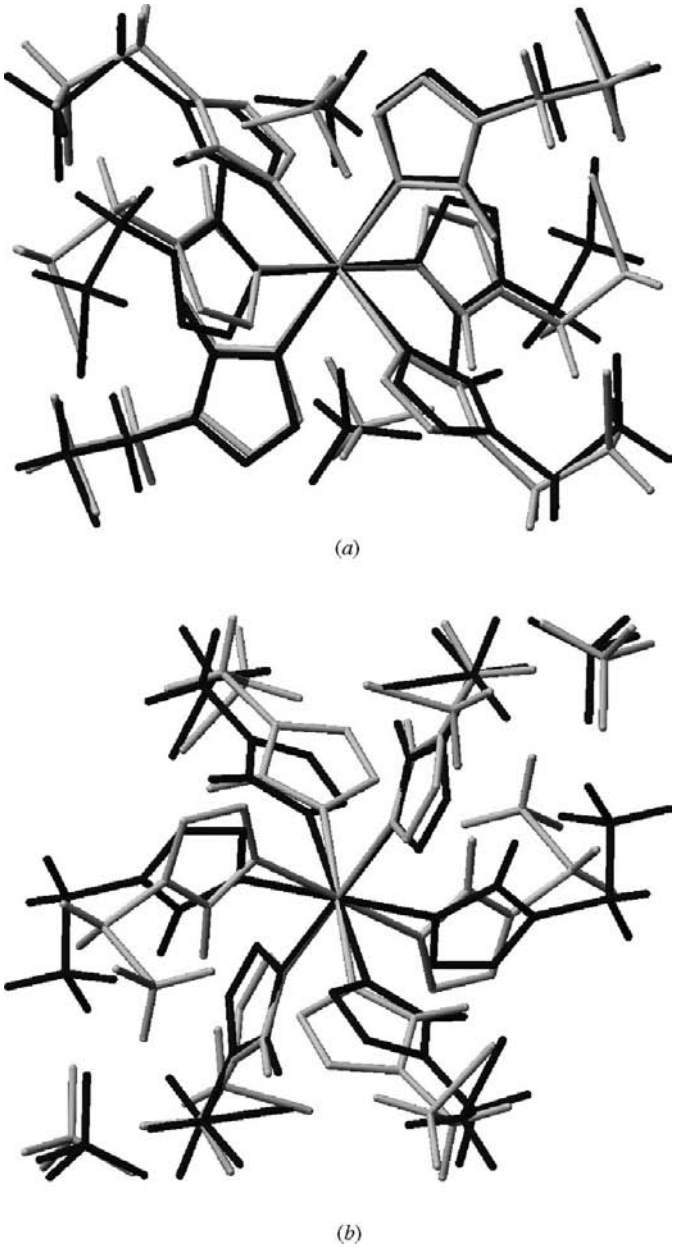

Figure 5
The structural models (*a*) M1 and (*b*) M2 of $[Fe(teeb)_6](BF_4)_2$ before (light grey) and after (dark grey) RR with *GSAS*.

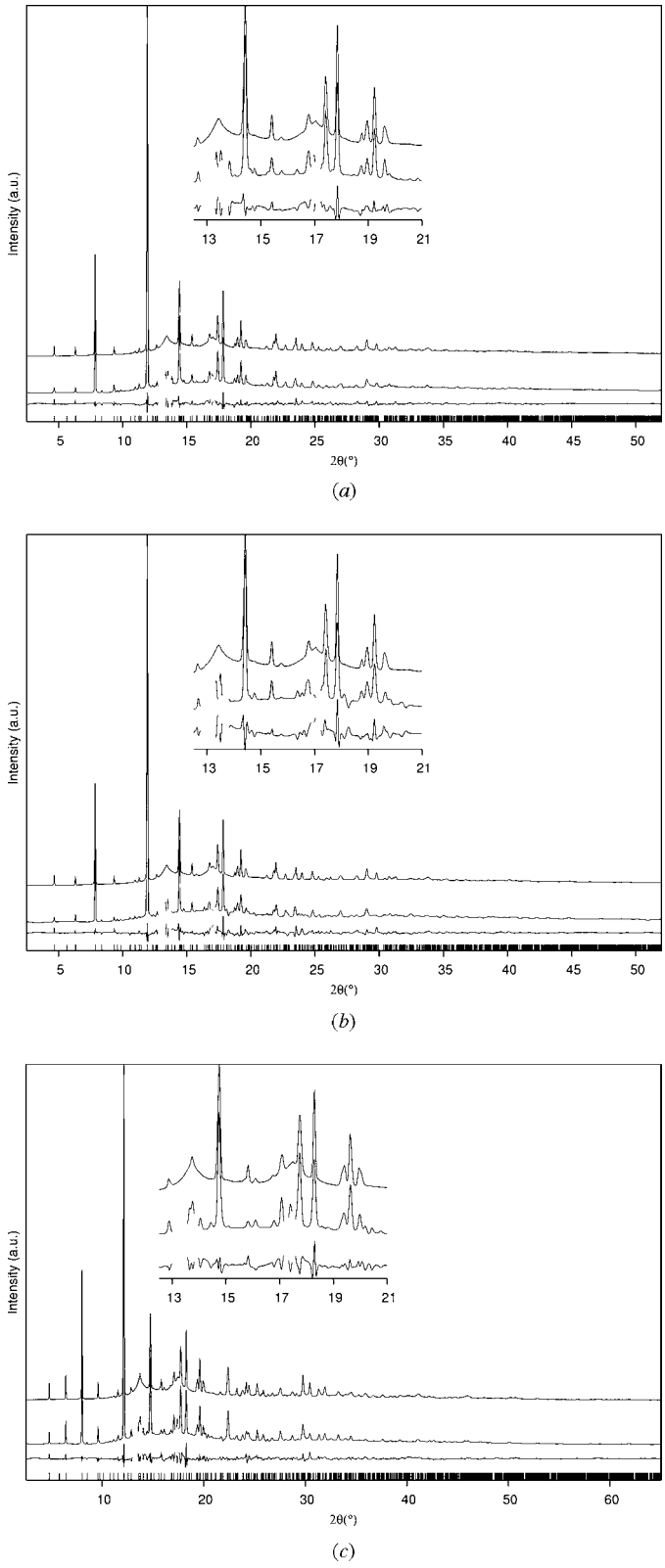

Figure 6
Rietveld refinement (*GSAS*) plots of the $[Fe(teeb)_6](BF_4)_2$ structures (*a*) at 300 K (M1), (*b*) at 300 K (M2) and (*c*) at 90 K: experimental diffraction pattern (upper), the pattern as calculated from the refined crystal structure (middle), the difference between these patterns (lower) and reflection positions (vertical lines).

4.4. Crystal structure analysis

4.4.1. *Teei*. As in *teec*, the Fe^{II} atom in *teei* is at a special position and is octahedrally coordinated by the neighbouring N atoms at distances of 2.200 (15)–2.219 (15) Å at RT and 1.873 (17)–2.046 (18) Å at 90 K; these are typical Fe—N distances for HS and LS states, respectively (König, 1987).

The mean bond distance of the Fe moiety (excluding the Fe—N bonds) is 1.31 Å at RT and 1.28 Å at 90 K, corresponding to a shrinkage of 2.1% due to temperature. When only Fe—N bond distances are considered (mean Fe—N bond contraction of 0.25 Å), the decrease is 11.2%. From the above it is concluded that the prominent shortening of the Fe—N bond distances as the temperature decreases, in contrast to the much smaller shortening of the other bond distances, can be attributed to the HS → LS transition. [Distances and angles given in the text containing s.u. values have been calculated with the program *PLATON* (Spek, 2001); those not containing s.u values have been calculated with *DIAMOND* (Pennington, 1999; Cordier, 1999) or *PLUVA* (Driessen *et al.*, 1988); selected bonds and angles of *teei* at RT and 90 K are given in Table 5.] Because a restrained RR was applied in all cases, bond distances and angles values should be considered as approximate and not absolute.

Table 6
Possible intermolecular hydrogen bonds (Å, °) of the $[Fe(teei)_6](BF_4)_2$ structures at RT and 90 K.

	RT			90 K		
	N···H	N···C	N—H—C	N···H	N···C	N—H—C
N2*a*···H2*b*2—C2*b*	2.30 (3)	3.32 (3)	151 (3)	2.73	3.65	150
N2*b*···H2*a*1—C2*a*	2.46 (2)	3.22 (3)	125 (2)	2.67	3.08	103
N2*c*···H2*c*1—C2*c*	2.55 (3)	3.32 (3)	128 (2)	3.36	3.64	98
N3*a*···H2*b*2—C2*b*	2.84	3.66	130	3.26	4.07	137
	I···H	I···C	I—H—C	I···H	I···C	I—H—C
I1···H3*c*2—C3*c*	3.03 (4)	3.96 (3)	142 (3)	3.36	4.29	141
I3···H3*b*1—C3*b*	3.13	4.03	147	2.89 (7)	3.48 (3)	116

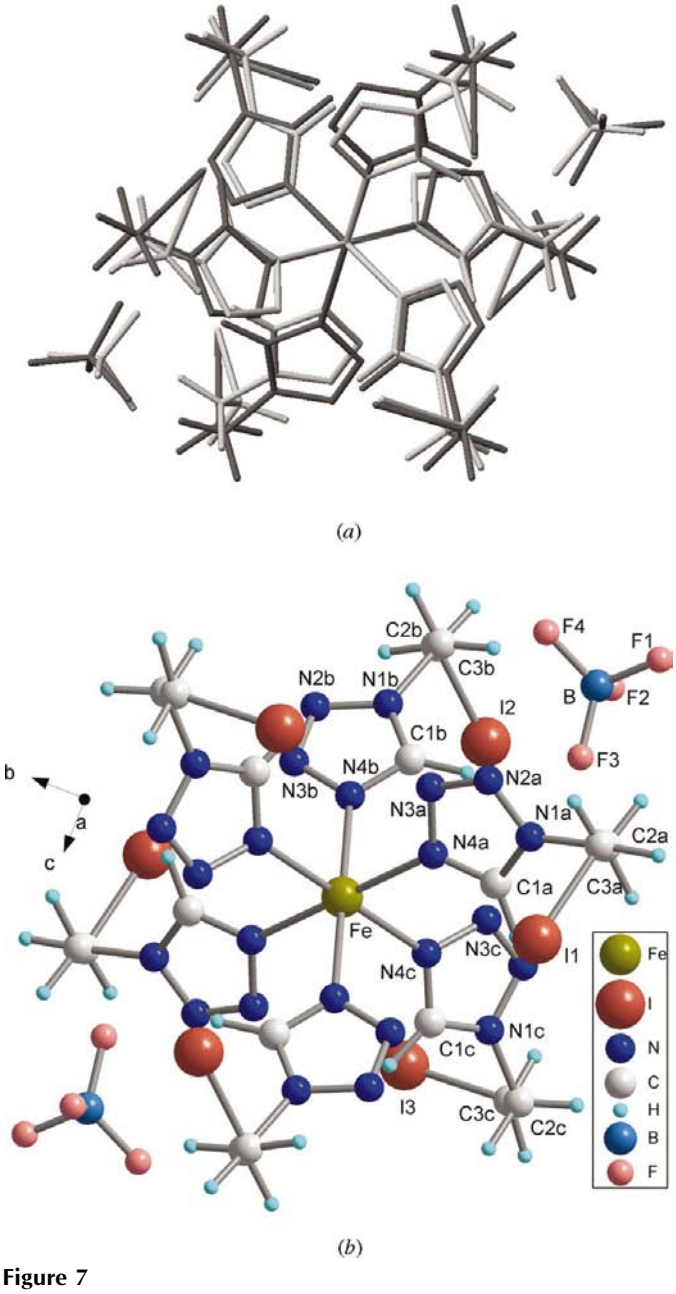

Figure 7
(*a*) The refined structures of $[Fe(teei)_6](BF_4)_2$ at 300 (dark grey) and 90 K (light grey) superimposed. (*b*) The molecular crystal structure of $[Fe(teei)_6](BF_4)_2$ at 300 K showing the numbering scheme.

Fig. 7(*a*) shows a superposition of the refined structures of *teei* at 300 and 90 K. The molecular structure, with the numbering of the non-H atoms in the asymmetric unit, is shown in Fig. 7(*b*). From the superposition of the structures it is concluded that, apart from the shortening of the Fe—N bond distances, the tetrazole rings remain almost parallel to their initial orientation. In addition, the I atoms remain almost in their initial positions.

Like *teec*, *teei* is packed in layers along the unit-cell axes (Figs. 8 and 9). The differences between the structures at 300 and 90 K are much smaller than the corresponding differences in the *teec* complex (Dova, 2003). The distance between the structural layers is ∼2 Å at RT and slightly shorter at 90 K, and atoms involved in the closest contacts between the layers are I and H atoms. Two interlayer I···H—C hydrogen bonds, almost parallel to the *a* axis, are suggested by *PLATON*: one at RT and another at 90 K (Table 6). The I1···H3*c*2—C3*c* hydrogen bond seems to become weaker at 90 K, while the I3···H3*b*1—C3*b* interaction becomes stronger. Possible intermolecular N···H—C hydrogen bonds are also listed in Table 6. From the N···H distances it can be concluded that more hydrogen-bond stabilization exists at RT than at 90 K.

4.4.2. Teeb. In view of the quality of the crystal structure determination of *teeb*, only the main structural features will be discussed. As in all previous complexes, the Fe atom in the centrosymmetric *teeb* complex is at a special position and is octahedrally coordinated by the neighbouring N atoms. The Fe—N bond distances and angles at both temperatures are listed in Table 5. The average Fe—N bond shrinkage is 8%, which is comparable to the shrinkage observed in $[Fe(teec)_6](ClO_4)_2$ (Dova, 2003) and smaller than that

observed for *teei*. The Fe—N distances at 300 K are typical of the HS state, while the Fe—N4*a* and Fe—N4*c* at 90 K are slightly higher than the typical distances of the LS state.

In Fig. 10(*a*), the refined structures of *teeb* at 300 and 90 K are superimposed. The molecular structure, with the numbering of the non-H atoms of the asymmetric unit, is shown in Fig. 10(*b*). Like *teec* and *teei*, *teeb* is arranged in layers along the *b* and *c* axes, almost perpendicular to the *a* axis. The interlayer distance is approximately 2 Å (taking into account only the Br-atom positions). The C—Br bonds are arranged almost parallel to the *bc* plane. The BF_4^- moieties are arranged in layers, with the *x* coordinate of B close to 0.

4.4.3. Spin-crossover behaviour. In both *teei* and *teeb*, the SCO is gradual and complete. From the superposition of the

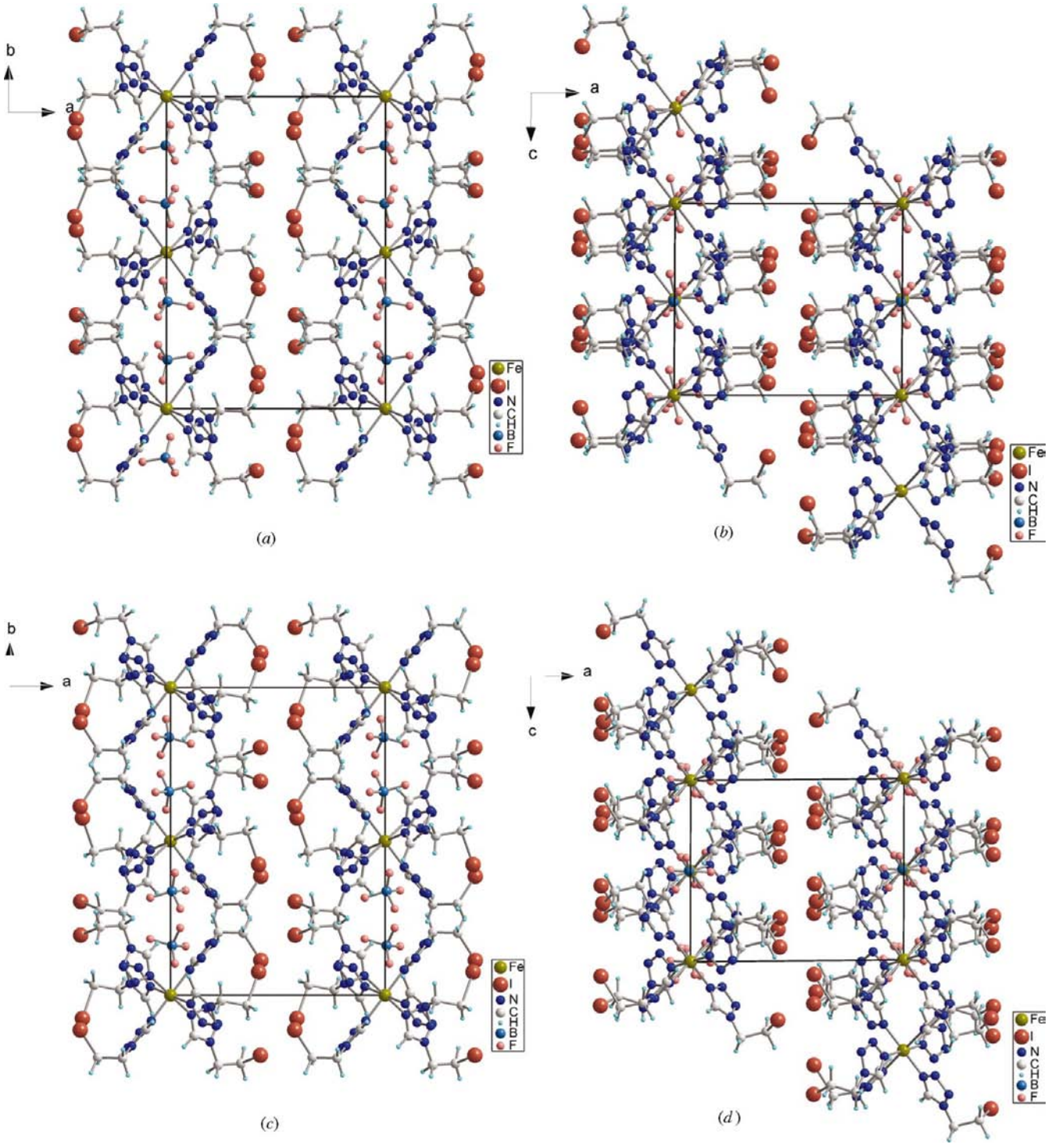

Figure 8
The structure of $[Fe(teei)_6](BF_4)_2$ at (*a*), (*b*) RT and (*c*), (*d*) 90 K showing the layers formed along the *b* and *c* axis [(*a*), (*c*) and (*b*), (*d*), respectively], perpendicular to the *a* axis.

teei structures at RT and 90 K it is concluded that, apart from the Fe—N bond contraction, the orientations of the tetrazole rings have hardly changed, being almost parallel at both temperatures. These gradual, smooth and small structural changes can also be inferred from the diffraction patterns of the scan measurements, in which no obvious appearance of new peaks or fading of existing peaks could be detected. Comparing the scan and the long-term measurements of *teei* at the same temperature, the only clear difference was an overall lower sharpness of the intensity peaks in the scan measurements; this difference may have been caused by the extensive grinding of that particular sample. From the above, it seems that, at least at the time scale of the performed experiments, the formation of distinct domains with similar spins, large enough to give a distinguishable diffraction pattern, does not occur in *teei* and *teeb*; their SCO behaviour seems to be more consistent with the regular solution theory, according to which both the electronic and the structural changes evolve gradually and smoothly.

SCO behaviour (gradual, complete single-step) and structural characteristics ($P2_1/c$) similar to that of *teei* and *teeb* have been found in, amongst others, $Fe(PM\text{-}AzA)_2(NCS)_2$ [AzA is 4-(phenylazo)aniline and PM is *N*-2′-pyridylmethylene; Guionneau *et al.*, 1999]. This compound also exhibits a lattice contraction when the temperature is lowered, the Fe—N bond contraction ranging from Fe—N(CS) = 0.11 Å to Fe—N(phenyl) = 0.28 Å (mean 0.19 Å). In contrast to the situation in *teei* and *teeb*, the Fe^{II} atom is at a general position and the

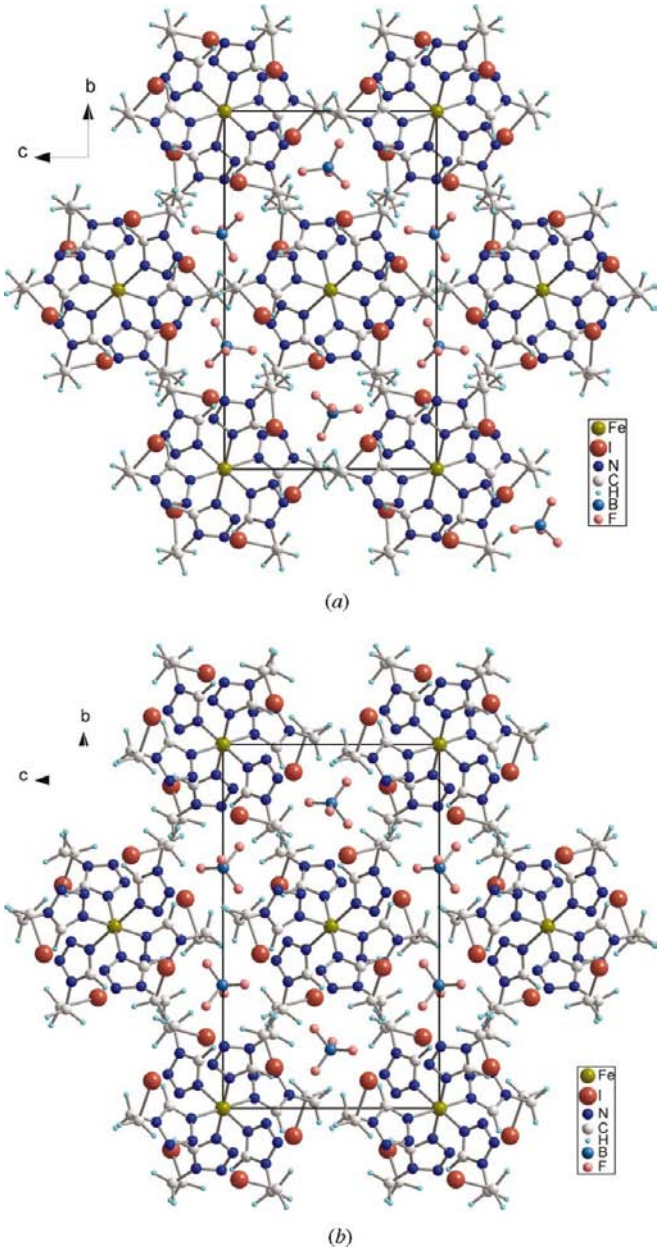

Figure 9
A view of the structure of $[Fe(teei)_6](BF_4)_2$ at (*a*) RT and (*b*) 90 K along the *a* axis; within these layers the Fe and B atoms exhibit a pseudo-trigonal symmetry.

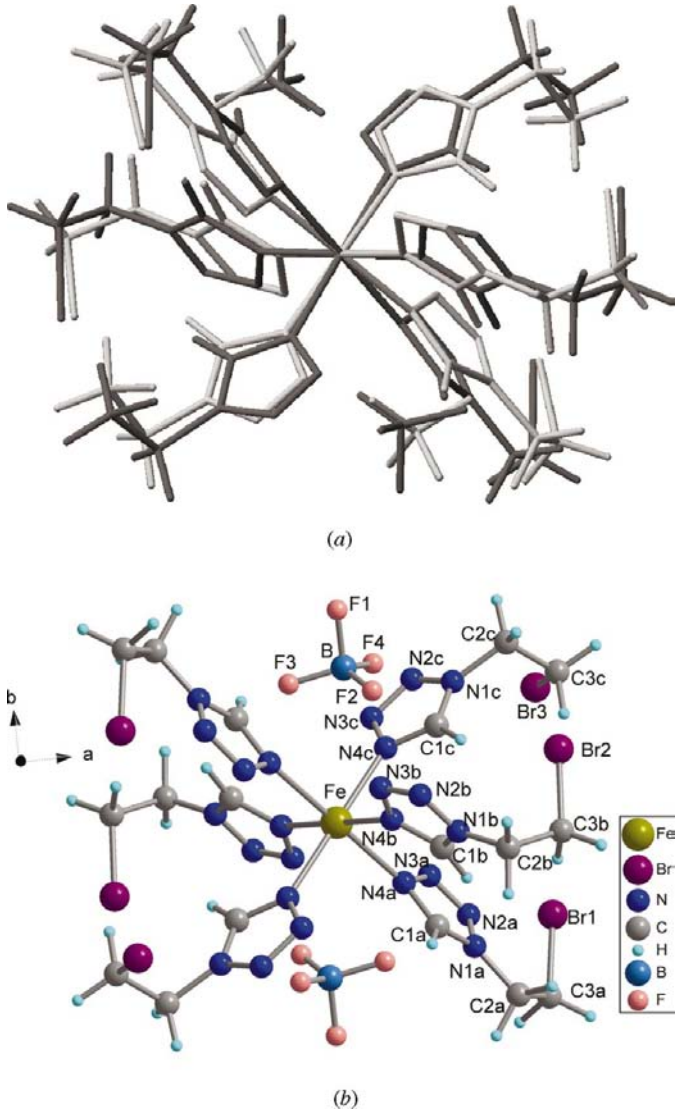

Figure 10
(*a*) The refined structures at 300 (dark grey) and 90 K (light grey) superimposed. (*b*) The molecular crystal structure of $[Fe(teeb)_6](BF_4)_2$ at 300 K showing the numbering scheme.

Fe—N sixfold coordination is more asymmetric, but these differences do not seem decisive for a change in SCO behaviour.

The authors would like to thank Drs Wouter van Beek and Herman Emerich (BM1B, SNBL) for their help during the powder diffraction measurements at the ESRF (Grenoble, France), and Professor Dr M. Takata and Dr E. Nishibori for their help during the experiments carried out at SPring8 (JASRI, Japan). ED acknowledges Accelrys Inc. for allowing the use of *Materials Studio* software for evaluation purposes. Matthias Grunert and Wolfgang Linert are thanked for synthesizing and providing the *teei* complex.

References

Accelrys (2001). *Materials Studio*. Accelrys Inc., 6985 Scranton Road, San Diego, CA 92121–3752, USA.
Ahtee, M., Nurmela, M., Suortti, P. & Järvinen, M. (1989). *J. Appl. Cryst.* **22**, 261–268.
Bérar, J.-F. & Baldinozzi, J. (1993). *J. Appl. Cryst.* **26**, 128–129.
Bolvin, H. & Kahn, O. (1995). *Chem. Phys. Lett.* **192**, 295–305.
Chernyshev, V. V. & Schenk, H. (1998). *Z. Kristallogr.* **213**, 1–3.
Cordier, G. (1999). *Nachr. Chem. Tech. Lab*. **47**, 1437–1438.
Decurtins, S., Gütlich, P., Hasselbach, K. M., Hauser, A. & Spiering, H. (1985). *Inorg. Chem.* **24**, 2174–2178.
Decurtins, S., Gütlich, P., Spiering, H., Hauser, A. & Köhler, C. P. (1984). *Chem. Phys. Lett.* **105**, 1–4.
Dova, E. (2003). PhD thesis, University of Amsterdam, The Netherlands.
Dova, E., Stassen, A. F., Driessen, R. A. J., Sonneveld, E., Goubitz, K., Peschar, R., Haasnoot, J. G., Reedijk, J. & Schenk, H. (2001). *Acta Cryst.* B**57**, 531–538.
Driessen, R. A. J., Loopstra, B. O., de Bruijn, D. P., Kuipers, H. P. C. E. & Schenk, H. (1988). *J. Comput. Aided Mol. Des.* **2**, 225–233.
Engel, G. E., Wilke, S., Köning, O., Harris, K. D. M. & Leusen, F. J. J. (1999). *J. Appl. Cryst.* **32**, 1169–1179.
Guionneau, P., Letard, J.-F., Yufit, D. S., Chasseau, D., Bravic, G., Goeta, A. E., Howard, J. A. K. & Kahn, O. (1999). *J. Mater. Chem.* **9**, 985–994.
Gütlich, P., Garcia, Y. & Godwin, H. A. (2000). *Chem. Soc. Rev.* **6**, 419–427.
Gütlich, P. & Hauser, A. (1990). *Coord. Chem. Rev.* **97**, 1–22.
Gütlich, P., Hauser, A. & Spiering, H. (1994). *Angew. Chem. Int. Ed. Engl.* **33**, 2024–2054.
Järvinen, M. (1993). *J. Appl. Cryst.* **26**, 525–531.
Kahn, O. & Jay Martinez, C. (1998). *Science*, **279**, 44–48.
König, E. (1987). *Prog. Inorg. Chem.* **35**, 527–623.
Koudriavtsev, A. B., Stassen, A. F., Haasnoot, J. G., Grunert, M., Weinberger, P. & Linert, W. (2003*a*). *Phys. Chem. Chem. Phys.* **5**, 3666–3675.
Koudriavtsev, A. B., Stassen, A. F., Haasnoot, J. G., Grunert, M., Weinberger, P. & Linert, W. (2003*b*). *Phys. Chem. Chem. Phys.* **5**, 3676–3683.
Kröber, J., Codjovi, E., Kahn, O., Grolière, F. & Jay, C. (1993). *J. Am. Chem. Soc.* **115**, 9810–9811.
Larson, A. C. & Von Dreele, R. B. (1994). *GSAS*. Report No. LAUR 86–748. Los Alamos National Laboratory, New Mexico, USA.
Megaw, H. D. (1934). *Nature* (*London*), **134**, 900–901.
Meissner, E., Köppen, H., Spiering, H. & Gütlich, P. (1983). *Chem. Phys. Lett.* **95**, 163–166.
Nishibori, E., Takata, M., Kato, K., Sakata, M., Kubota, Y., Aoyagi, S., Kuroiwa, Y., Yamakata, M. & Ikeda, N. (2001). *Nucl. Instrum. Methods Phys. Res. A*, **467–468**, 1045–1048.
Onishi, S. & Sugano, S. (1981). *J. Phys. C Solid State Phys.* **14**, 39–55.
Pennington, W. T. (1999). *J. Appl. Cryst.* **32**, 1028–1029.
Real, J. A., Castro, I., Bousseksou, A., Verdaguer, M., Burriel, R., Castro, M., Linares, J. & Varret, F. (1997). *Inorg. Chem.* **36**, 455–464.
Slichter, C. P. & Drickamer, H. G. (1972). *J. Chem. Phys.* **56**, 2142–2160.
Sorai, M. & Seki, S. (1974). *J. Phys. Chem. Solids*, **35**, 555–570.
Spek, A. L. (2001). *PLATON*. Utrecht University, The Netherlands.
Spiering, H., Meissner, E., Köppen, H., Müller, E. W. & Gütlich, P. (1982). *Chem. Phys.* **68**, 65–71.
Stassen, A. F. (2002). PhD thesis, Leiden University, The Netherlands.
Stassen, A. F., Dova, E., Ensling, J., Schenk, H., Gütlich, P., Haasnoot, J. G. & Reedijk, J. (2002). *Inorg. Chim. Acta*, **335**(C), 61–68.
Stassen, A. F., Grunert, M., Dova, E., Schenk, H., Wiesinger, G., Linert, W., Haasnoot, J. G. & Reedijk, J. (2003). *Eur. J. Inorg. Chem.* pp. 2273–2282.
Toby, B. H. (2001). *J. Appl. Cryst.* **34**, 210–213.
Toraya, H. (1986). *J. Appl. Cryst.* **19**, 440–447.
Visser, J. W. (1969). *J. Appl. Cryst.* **2**, 89–95.
Zlokazov, V. B. & Chernyshev, V. V. (1992). *J. Appl. Cryst.* **25**, 447–451.